Article

Low-Temperature Highly Robust Hydrogen Sensor Using Pristine ZnO Nanorods with Enhanced Response and Selectivity

Chandra Prakash, Rajneesh Chaurasiya, Abhijeet J. Kale, and Ambesh Dixit*

Read Online

ACCESS | Metrics & More | Article Recommendations | Supporting Information

ABSTRACT: We report the hydrogen-sensing response on low-cost-solution-derived ZnO nanorods (NRs) on a glass substrate, integrated with aluminum as interdigitated electrodes (IDEs). The hydrothermally grown ZnO NRs on ZnO seed-layer-glass substrates are vertically aligned and highly textured along the c-axis (002 plane) with texture coefficient ~2.3. An optimal hydrogen-sensing response of about 21.46% is observed for 150 ppm at 150 °C, which is higher than the responses at 100 and 50 °C, which are ~12.98 and ~10.36%, respectively. This can be attributed to the large surface area of ~14.51 m^2/g and pore volume of ~0.013 cm^3/g, associated with NRs and related defects, especially oxygen vacancies in pristine ZnO nanorods. The selective nature is investigated with different oxidizing and reducing gases like NO_2, CO, H_2S, and NH_3, showing relatively much lower ~4.28, 3.42, 6.43, and 3.51% responses, respectively, at 50 °C for 50 ppm gas concentration. The impedance measurements also substantiate the same as the observed surface resistance is initially more than bulk, which reduces after introducing the hydrogen gas during sensing measurements. The humidity does not show any significant change in the hydrogen response, which is ~20.5 ± 1.5% for a large humidity range (from 10 to 65%). More interestingly, the devices are robust against sensing response, showing no significant change after 10 months or even more.
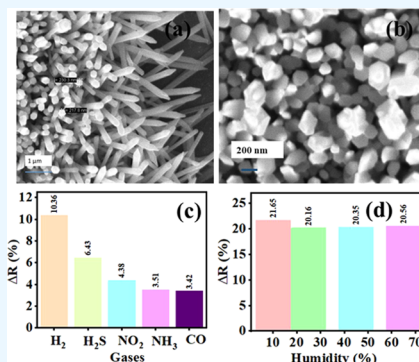
INTRODUCTION

Hydrogen is one of the promising alternatives to exhausting conventional energy sources like fossil fuels, e.g., coal, petroleum, etc., and is attracting attention as the future fuel for zero emission. Its potential and earth abundancy have been well recognized in the industrial domain since 1970 to reduce the energy dependency over polluting conventional energy resources.[1] It is considered a better replacement for fossil fuels because of its unique characteristics, such as complete recyclability and being pollution-free. It is currently used in aerospace, power generator, fuel cell, and automobile applications.[2,3] The strong reducing characteristics of hydrogen make it very useful in semiconductor processing, glass-making, and chemical industries.[4] However, its use leads to several challenges in its detection as it is the lightest element in the periodic table and is odorless, colorless, and tasteless.[5] Further, the highly flammable nature of hydrogen, even at 4% concentration in air, poses challenges to its safe handling and uses. Thus, there is a high tendency for its leakage, which may lead to explosions under certain conditions.[6] All of these threats associated with hydrogen compel us to innovate an efficient hydrogen gas sensor, which can detect low concentrations (in ppm or ppb) with enhanced efficiency at low temperatures in conjunction with high retentivity and selectivity. Additionally, these sensors should be economical, i.e., have low material cost, be easy to fabricate, have low power consumption, and possess enhanced environmental stability.[6,7]

Hydrogen gas sensors are commonly based on metal oxide semiconductors (MOS), such as zinc oxide (ZnO), tungsten oxide (WO_3), titanium oxide (TiO_2), cerium oxide (CeO_2), copper oxide (CuO), tin oxide (SnO_2), and nickel oxide (NiO).[1,8,9] These metal oxide materials are usually large band-gap materials, including a wide range, i.e., semiconducting to insulating materials.[10] MOS exhibit better stability under ambient conditions and offer excellent physical, chemical, mechanical, optical, and electronic properties. They are easy to synthesize in different geometries using numerous techniques such as sol−gel spin coating, pulse laser deposition (PLD), sputtering, electrochemical, hydrothermal, thermal evaporation techniques, etc.[11] The hydrothermal technique is widely used for synthesizing nanostructures even at a much lower working temperature range, i.e., between 70 and 150 °C, compared to other techniques.[12] Metal oxides are preferred for gas-sensing applications, but they have some drawbacks including considerable response time, low response, significant recovery time, selectivity, and higher operating temperatures.
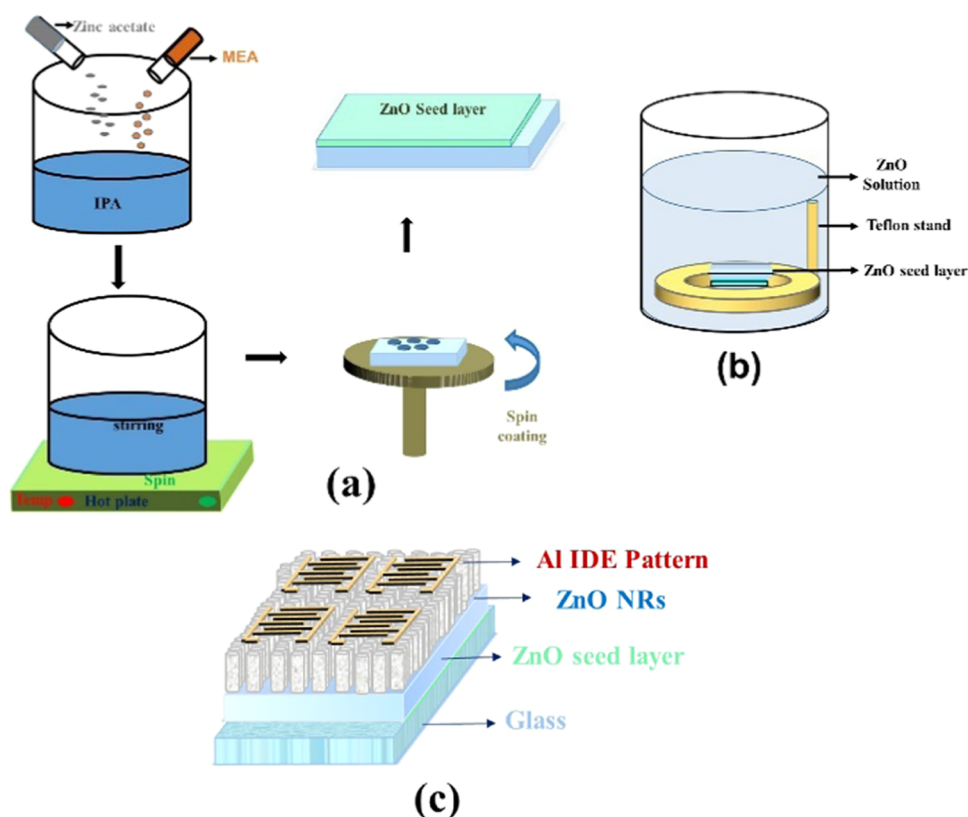
Figure 1. Schematic diagram explaining the synthesis of (a) ZnO seed layer, (b) ZnO nanorods on seed-layered glass substrate, and (c) aluminum IDE patterns on ZnO NRs/glass for sensing hydrogen gas.

Zinc oxide, among other MOS materials, has attracted attention because of its specific optoelectronic properties such as large exciton binding energy (60 meV), wide band gap (3.37 eV), large bulk modulus (~142 GPa), moderate dielectric constant, high chemical stability, high electron mobility, and nontoxic nature.[13−17] Despite these advantages, pristine ZnO as a sensing material suffers from a low response and requires high operating temperatures. These properties can be enhanced by doping with other metals such as nickel, cobalt, copper, aluminum, etc., or by heterostructuring it with other functional materials or functionalizing it with noble metals like Pt and Au.[11,18−20] There are several studies on ZnO NR-based hydrogen gas sensors; e.g., Abun et al.[21] synthesized ZnO NRs using sputtering and hydrothermal processes and showed 10% response at 25 °C for 500 ppm gas concentration. Further, the authors showed enhanced response (~60%) at the same temperature and gas concentration by heterostructuring it with MoSe$_2$, MoSe$_2$ NPs/ZnO NRs as p−n junctions. Cittadini et al. reported hydrogen gas sensing on ZnO NRs containing Pt particles; Fan et al. showed hydrogen sensor response on ZnO nanorods and Pt-Au-loaded ZnO NRs, synthesized using the sol−gel process. The response was enhanced from 1% on ZnO NRs to 157.4% for Pt-Au-loaded ZnO NRs at 130 °C and 250 ppm hydrogen. Sett et al. reported 11% sensing response on pristine ZnO, which increased to 57.3% for Co-doped ZnO NRs at 150 °C with 3000 ppm gas concentration. The enhancement in hydrogen response can be attributed to the increase in oxygen vacancies after Co doping in ZnO NRs.[18,22,23] Das et al.[24] found an extremely high sensing response of 586.93% for 100 ppm gas concentration at room temperature with a fast response (17.02 s) and recovery time (27.06 s) on reduced graphene oxide (rGO)-modified ZnO

NRs. Kumar et al.[25] fabricated Pd-loaded ZnO NR-based highly selective hydrogen gas sensors and showed a low limit of detection up to 7 ppm with 38.7% response at 175 °C. However, less emphasis is given to developing pristine ZnO NRs, i.e., without its doping and functionalization. Some reports, for example, Agarwal et al.,[26] showed that pristine ZnO NRs do not show any significant hydrogen response up to 150 °C and 300 ppm gas concentration, which further increases with increasing temperature after silver "Ag" modification. Cheng et al.[27] showed 1.7% hydrogen gas response on ZnO at a relatively higher temperature (~250 °C) and 15 ppm gas concentration, which further improved to ~4.8% after decorating with Pt on ZnO NRs.

This paper reports the synthesis of highly textured c-axis-oriented ZnO nanorods integrated with non-noble aluminum metal as the interdigitated electrode (IDE) pattern and their hydrogen-sensing characteristics together with the influence of numerous factors such as operating temperature range from 50 to 150 °C, stability of the device, response and recovery time, and gas concentration. Further, the selective nature of the ZnO NRs is investigated against the potential oxidizing and reducing gas. The impact of humidity is evaluated by exposing hydrogen gas under highly moist conditions. Hydrogen sensing of ZnO nanorods is analyzed in terms of change in resistance during the adsorption of H$_2$ at different temperatures.

■ EXPERIMENTAL DETAILS

The synthesis steps for highly textured ZnO nanorods and interdigitated electrodes for electrical measurements are described in the following subsections.
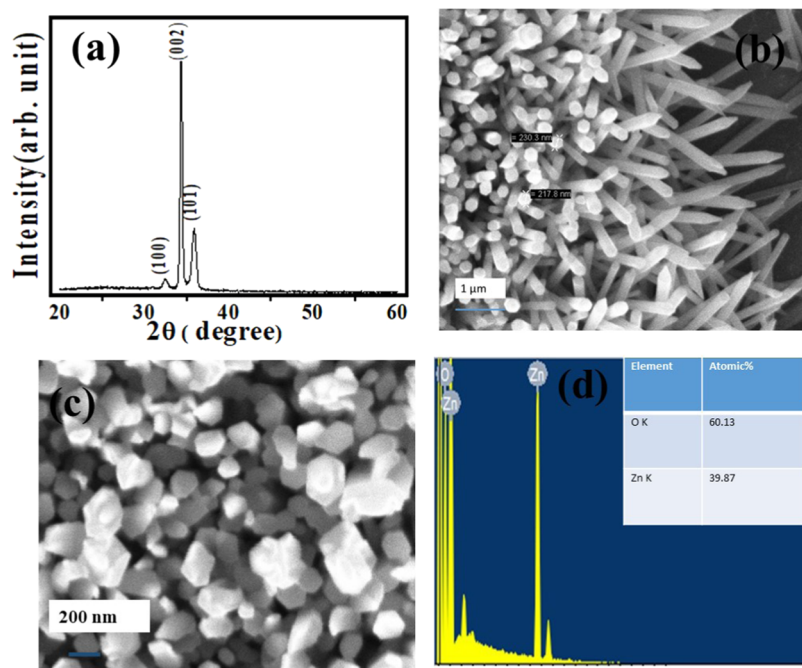
Figure 2. (a) X-ray diffraction pattern and scanning electron microscopic images for ZnO nanorods showing the (b) side view, (c) high-magnification surface microscopic images, and (d) energy-dispersive X-ray (EDX) measurement, showing atomic fractions.

ZnO Seed Layer. Zinc acetate dihydrate (10 mM) and monoethanolamine (10 mM) are dissolved in 10 mL of isopropyl alcohol (IPA), as explained schematically in Figure 1a. This solution is continuously stirred for 3 h to obtain a uniform mixture, followed by room-temperature aging for 24 h. The aged solution is spin-coated on a glass substrate at 3000 rpm for 30 s. The spin-coated glass substrate is then subjected to preheating on a hot plate at 300 °C for 2−3 min to remove the residual organics. The spin coating and subsequent preheating processes are repeated five times to achieve the desired thickness of the seed layer, which is finally calcinated at 450 °C for 4 h in a box furnace under ambient conditions. All of these steps are explained in Figure 1a schematically.

Growth of ZnO Nanorods. Zinc acetate dihydrate (25 mM) as a Zn source and hexamethylenetetramine (HMTA) (25 mM) as the chemical reagent, essential for NR growth, are mixed in 300 mL of deionized water. The solution is continuously stirred at room temperature for 1 h to get the homogeneous solution, as shown schematically in Figure 1b. The seed-layer-integrated glass substrate is kept on a Teflon stand, facing downward in this solution, Figure 1b. This solution is placed in an electric oven for 6 h at 95 °C. After that, the substrate is allowed to cool down to room temperature and washed with DI water. It is finally heated at 450 °C for 4 h in a box furnace under ambient conditions to get the *c*-axis-oriented zinc oxide nanorods.

Device Fabrication. Aluminum (Al) is used as the contact material for electrical measurements. A shadow mask consisting of an interdigitated electrode (IDE) pattern is placed on the grown ZnO nanorods and kept in a thermal evaporation system. The base pressure of the system is maintained at 10^{-5} mbar before deposition. The distance between adjacent strips/layers in the Al IDE shadow mask is 300 μm with a 550 μm width, and the length is 7.5 mm. The thickness of the deposited Al IDEs is ∼150 nm. The IDEs on

the ZnO NRs/glass substrate are shown schematically in Figure 1c.

Sensing Measurement. An in-house sensing setup is developed with respective components for making it semi-automated. It consists of a gas chamber with vacuum systems for evacuating the chamber whenever required. The gas chamber is maintained at 0.010−0.015 mbar pressure throughout the experiment using a rotary pump. This low pressure, i.e., vacuum, inside the enclosed gas chamber assists in isolating the sensing measurement with the environmental perturbations. The gas lines are connected with the test chamber, and electrical feedthrough from the test chamber is connected with a Keithley source meter or Metrohm electrochemical workstation for electrical measurements with and without gas in the chamber. The system is semiautomated for recording data. H_2 gas is released at 100, 50, and 25 ppm for both 100 and 50 °C temperatures in a sequential order for its sensing. The corresponding change in current is measured using a Keithley source meter (6517B). The device's response to H_2 gas is then analyzed by calculating the ratio of resistance in the presence of a gas to the resistance in air or before adsorbing the gas on the device. Further, to understand the impact of relativity on hydrogen-sensing response, controlled water vapors are introduced in the chamber together with the target gas. The relativity humidity is continuously monitored during the measurements using a humidity sensor HT−306.

Characterization of Materials and Devices. The phase purity of grown ZnO nanorods is confirmed using an X-ray diffractometer (Bruker make) with a Cu Kα source (wavelength ∼ 1.54 Å). The morphology, microstructure, and compositional analysis for ZnO nanorods are investigated by scanning electron microscopy (SEM) and energy-dispersive X-ray (EDX) (Zeiss make). The optical band gap is measured using a UV−vis spectrometer in the 400−800 nm range. The vibrational modes are investigated using FTIR (Bruker) in the 400−4000 cm^{-1} wavenumber range. The room-temperature
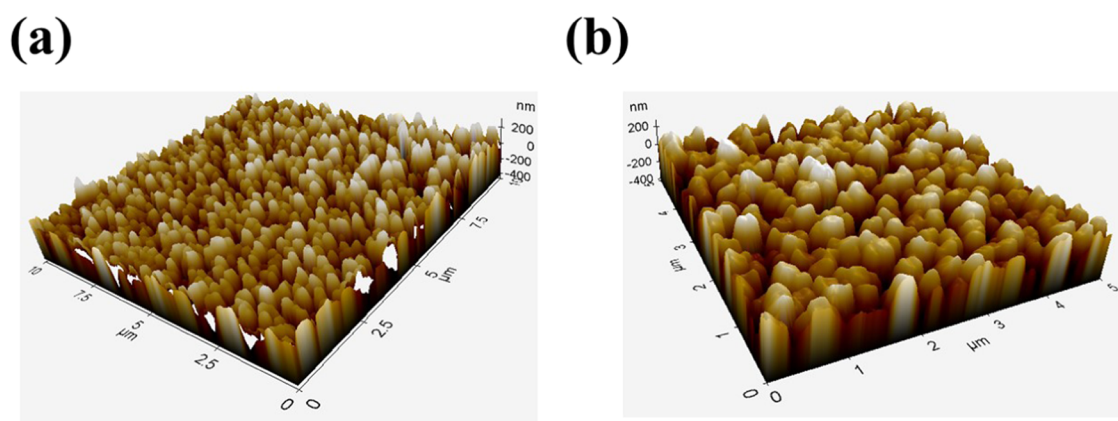
Figure 3. Three-dimensional AFM images for vertically aligned pristine ZnO NRs grown on the ZnO seed layer on a glass substrate: (a) 10 μm $\times$ 10 μm area and (b) 5 μm $\times$ 5 μm.

photoluminescence is carried out to understand the defect, especially oxygen vacancies, in synthesized ZnO NRs. The specific surface area and pore size distribution are investigated using the Brunauer, Emmett, and Teller (BET) surface area analyzer technique using N_2 adsorption/desorption processes. The device impedance is characterized using the Metrohm electrochemical workstation in potentiostat and galvanostate configurations.

RESULTS AND DISCUSSION

Structural and Microstructural Analyses. The X-ray diffraction (XRD) measurement is carried out in the locked-coupled mode in the 20–60° 2θ range with a step size of 0.02 and a 2°/min scan rate using Cu Kα (1.54 Å) radiation, and the collected diffractogram is shown in Figure 2a. The diffraction peaks at 2θ = 32.51, 34.44, and 35.93° correspond to (100), (002), and (001) planes, respectively, consistent with reference ICDD #36-1481 for a hexagonal (wurtzite) structure. The corresponding lattice parameters are $a = b = 3.28$ Å and $c = 5.31$ Å, in agreement with the reported values.[28] The highest intensity for the (002) diffraction peak suggests that grown ZnO nanorods are highly textured along the *c*-axis. The computed texture coefficient $T_{c(hkl)} = \frac{I_{(hkl)} / I_{0(hkl)}}{(1/N) \sum_N I_{(hkl)} / I_{0(hkl)}}$ (where $T_{c(hkl)}$ is the texture coefficient of the plane (hkl), $I_{(hkl)}$ is the measured intensity, $I_{0(hkl)}$ is the (hkl) plane intensity from an ICCD-PDF reference data, and N is the number of reflections) is relatively high ($\sim$2.3) for the (002) orientation compared to other planer orientations. This is consistent with the recorded scanning electron microscopic images, as shown in Figure 2. The side view of grown ZnO nanorods is shown in Figure 2b, suggesting the hexagonal features. The random alignment is due to the breaking of the sample for precise edge imaging. High-resolution SEM image of the top view of the grown ZnO nanorods is shown in Figure 2c, explaining the vertically aligned and highly dense nanorods over the entire glass substrate. These nanorods are $\sim$6 μm long, having diameters of $\sim$200–250 nm approximately. The collected energy-dispersive X-ray spectrum is shown in Figure 2d, with the inset showing the atomic fractions, suggesting a relatively higher atomic fraction for oxygen. This higher oxygen atomic fraction relative to zinc is attributed to the surface-adsorbed oxygen in these NRs during annealing under ambient conditions, and no other element is detected in the EDX spectra, suggesting the purity of these synthesized ZnO NRs.

Further, three-dimensional (3D) AFM images of ZnO nanorod surfaces are collected for 10 μm $\times$ 10 μm and 5 μm $\times$ 5 μm areas to investigate the surface topography and roughness and are shown in Figure 3a,b. These micrographs also suggest the dense growth of highly oriented and vertically aligned hexagonal-shaped ZnO nanorods. The estimated average surface roughness and root-mean-square values are $\sim$77.48 and 97.11 nm, respectively. It is also expected that the enhanced surface roughness of ZnO NRs may provide a dynamic carrier path, which is used in lowering its free energy for ZnO nanorods. Further, the enhanced roughness may also provide more adsorption sites to the target gas on the ZnO nanorod surface.[29,30] The enhanced view of ZnO nanorods in the 5 μm $\times$ 5 μm AFM surface image (left panel) suggests the surface variation for these nanorods, which should be useful for additional adsorption sites.

Optical and Vibrational Measurements. We carried out absorption measurements on ZnO nanorods. The absorption spectrum shows a sharp peak at 378 nm (Supporting Figure S1a). Further, the absorption data is used to plot $(\alpha.E)^2$ vs energy (Supporting Figure S1b), and the sharp transition is extrapolated to zero of the $(\alpha.E)$,[2] and the estimated band gap is $\sim$3.2 eV, consistent with the reported literature.[31−33] Further, FTIR spectroscopic measurement is carried out in the transmission mode, and the recorded transmittance vs wavenumber is plotted for the 400−4000 cm^{-1} range (Supporting Figure S1c). Generally, metal oxides exhibit vibrational modes between 400 and 1200 cm^{-1} because of the interatomic vibrations in these oxides.[34] The vibration modes at 476 and 587 cm^{-1} are the characteristics of Zn−O modes.[35] Moreover, we also observed additional peaks at 2302 and 3687 cm^{-1} corresponding to O═C═O and O−H bonds, suggesting the presence of surface-adsorbed oxygen.

Photoluminescence. The photoluminescence (PL) spectrum is measured using a 320 nm excitation wavelength, and a sharp peak centered at 398 nm is observed, as shown in Figure 4 and marked with a vertical dashed line. This peak is attributed to the near band edge (NBE), which corresponds to the ZnO band gap. The asymmetry with broadness associated with the NBE peak signifies the presence of large defects in these ZnO NRs. In addition to NBE, a broad peak centered at 600 nm with a width of $\sim$75 nm is also observed, and its zoomed view is also shown as an inset in Figure 8. This broad peak is associated with defects, especially oxygen vacancies, which are the active donors in ZnO and responsible for
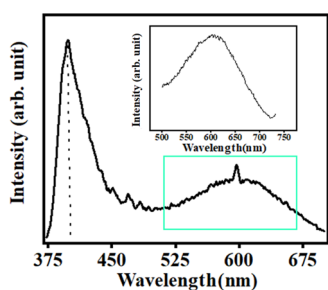
Figure 4. Room-temperature photoluminescence of ZnO NRs; the inset shows the zoomed-in view of a peak centered at 600 nm with a large width (∼75 nm).

chemisorption or dissociation of the oxygen molecule at the surface.[36−38]

Specific Surface Area. The specific surface area, pore size, and pore distribution are measured using the nitrogen adsorption/desorption Brunauer, Emmett, and Teller (BET) isotherm process for synthesized ZnO nanorods, and the results are summarized in Supporting Figure S3. The measured surface area of ZnO nanorods is ∼14.516 m^2/g, and the pore volume is 0.013 cm^3/g. These results agree with Kołodziejczak-Radzimska et al.'s reported work,[39] showing a surface area of ∼12.4 m^2/g for ZnO NRs, synthesized using the emulsion method. The average pore size distribution of ZnO nanorods is 1.8 nm, confirming that synthesized materials are porous at nanoscales.[40]

Sensing Characteristics. The sensing of metal oxide-based systems depends on the availability of oxygen molecule vacancies at a given temperature and the number of adsorbed molecules of the target gas.[3] Thus, the response $\Delta R(\%)$ of any material is given by $\Delta R(\%) = \frac{(R_{gas} - R_{air})}{R_{air}} \times 100$, where R_{gas} and R_{air} are resistances of the device under the target gas and air environments.[16]

The current−voltage (I−V) characteristics from −3 to 3 V are carried out to understand the hydrogen-sensing response at 50 and 100 °C in the test chamber in the presence of hydrogen gas at 25, 100, and 150 ppm. The recorded I−V characteristic curves are shown in Figure 5a,b for 50 and 100 °C temperatures. An apparent rise in the current is observed after introducing the gas in the test chamber.

The increase in current is attributed to the reaction between the target hydrogen gas molecules and surface oxygen adsorbate molecules on ZnO nanorods. This surface reaction produces excess electrons as $H_2 + O_{ads}^- \rightarrow H_2O + e^-$, thus resulting in enhanced current. Further, the resistance decreases
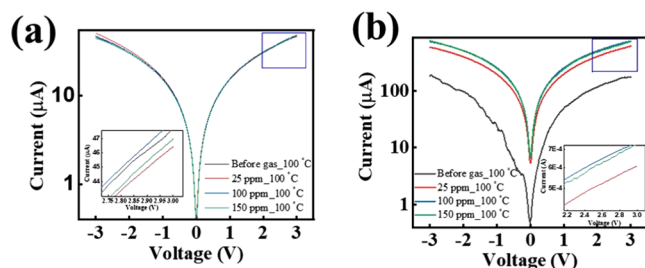
with increasing gas concentration. In the present work, the changes are more significant at higher temperatures, i.e., 100 °C. It is attributed to the increased O_2^- vacancies filled by the H_2 adsorbing molecules, thereby causing enhanced interaction sites, resulting in reducing resistance at higher temperatures. We also record the change in resistance vs time measurements at 2 V bias voltage by turning on and off the hydrogen gas at different concentrations for 50 and 100 °C temperatures with 10% relative humidity. At higher temperatures, the effect of humidity is negligible and does not show any significant change in the sensing response of the ZnO nanorods. The change in resistance is relatively low, exhibiting a moderate response of 5.41% with 12.5 ppm gas concentration at 50 °C (Figure 6a), which increases on increasing the concentration
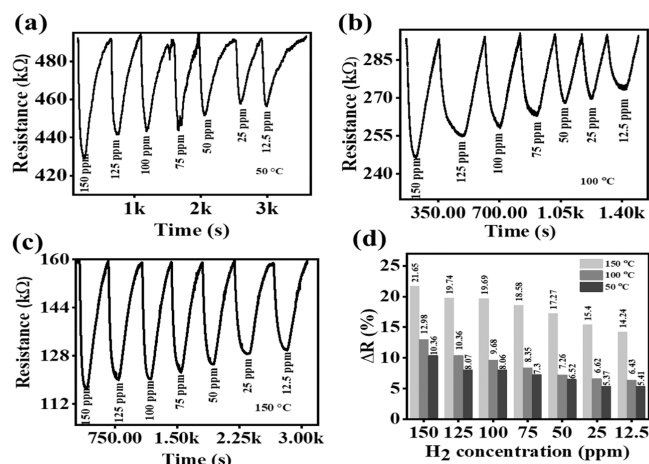
Figure 6. Gas-sensing response for ZnO NRs at (a) 50 °C, (b) 100 °C, (c) 150 °C for 150, 125, 100, 75, 50, 25, and 12.5 ppm H_2 concentrations. (d) Change in resistance against H_2 concentrations at fixed temperatures.

from 12.5 to 150 ppm. These changes are more significant at 100 and 150 °C as compared to that at 50 °C (Figure 6b,c). It is attributed to the increased oxygen vacancy sites at higher temperatures in ZnO NRs, providing more favorable sites for hydrogen gas adsorption, resulting in more considerable resistance change. The changes are significant from 12.5 to 150 ppm hydrogen concentration; however, at lower concentrations, change in resistance leads to saturation and a further decrease in concentration, as can be seen for 12.5 and 25 ppm concentrations for 50, 100, and 150 °C (Figure 6d). It may be due to less occupancy of available adsorbate sites while lowering the ppm level of hydrogen gas from 150 to 12.5 ppm. More interestingly, the enhancement in resistance change is noticed with increasing temperature for any gas concentration, i.e., the relative resistance change is more at 150 ppm for 150 °C, with a response of ∼21.45% as compared to 10.36 and 12.98% for 50 and 100 °C, respectively. It is attributed to the increased oxygen vacancies at higher temperatures because of thermal stimulation, essential for enhanced interaction with gas molecules.

The observed changes in resistance from these measurements are summarized in Figure 6d against hydrogen concentrations for different temperatures. The change in resistance is significant, nearly double, for a fixed hydrogen concentration at 150 °C (Figure 6d), which should increase further with increasing temperatures. Interestingly, the difference in resistance is relatively significant for lower concen-

Figure 5. Current−voltage (I−V) characteristics for ZnO NRs without and with 50, 100, and 150 ppm hydrogen gas concentrations at (a) 50 °C and (b) 100 °C, with the inset showing the zoomed-in view of the marked square.

trations, e.g., 12.5 ppm at 150 °C as compared to both 50 and 100 °C, which increases further with increasing gas concentration, e.g., 150 ppm.

We further estimated the response and recovery time against hydrogen concentration. The response time ($\tau_{response}$) is defined as the time taken by the sensor to reach 90% of the change in resistance to the initial resistance after exposing the target gas, whereas recovery time ($\tau_{recovery}$) is defined as the time the sensor takes to reach 10% of the initial resistance (i.e., the maximum resistance) after removing the target gas.[41] The results are summarized in Figure 7a,b, respectively, and in
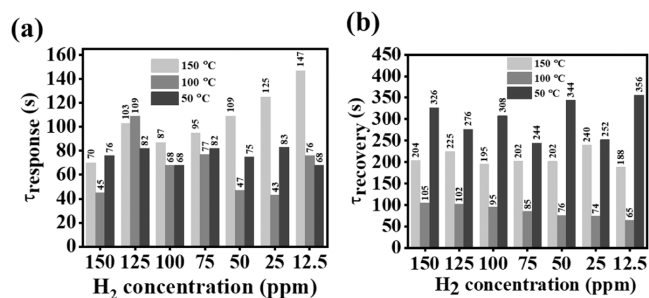
Figure 7. (a) Response time and (b) recovery time for ZnO NRs at different H$_2$ concentrations at 50, 100, and 150 °C.

Table 1. Response Time, Recovery Time, and Response for ZnO NRs at 50, 100, and 150 °C for Different Gas Concentrations

temperature (°C)	gas concentration (ppm)	response time (s)	recovery time (s)	response (ΔR) %
50	12.5	68	356	5.41
	25	83	252	5.37
	50	75	344	6.52
	75	82	244	7.30
	100	68	308	8.06
	125	82	276	8.07
	150	76	326	10.36
100	12.5	76	65	5.28
	25	43	74	6.52
	50	47	76	7.26
	75	77	85	8.35
	100	68	95	9.68
	125	109	102	10.36
	150	45	105	12.98
150	12.5	147	188	14.24
	25	125	240	15.40
	50	109	202	17.27
	75	95	202	18.58
	100	87	195	19.69
	125	103	225	19.74
	150	70	204	21.65

Table 1, together with the respective response for ZnO nanorods. The response time for ZnO NRs at 150 °C is 147 s for 12.5 ppm gas concentration, which is reduced to 70 s for 150 ppm gas concentration at the same temperature. The lowering of response time is attributed to the increased hydrogen adsorption on the nanorods' surface, making the response relatively faster. The recovery time is somewhat lower

at 100 °C (∼65 and 105 s) as compared to that at 50 °C (∼356 and 326 s) for (12.5 and 150 ppm) gas concentrations (Figure 7b). It suggests that ZnO NRs react with adsorbing gas molecules, i.e., hydrogen, much faster at lower temperatures because of more oxygen vacancies in the pristine system. Figure 7b shows that the observed recovery time is relatively larger than the response time for ZnO nanorods. The considerable recovery time is attributed to the large length of ∼6 μm, resulting in longer carrier dynamics over the length. However, the values are comparable to the reported recovery time. Catalysts like Pd and Pt are commonly used to reduce the recovery time for hydrogen sensors to achieve a better response, which is achieved in pristine ZnO NRs in the present study.[42,43]

Its selective nature plays an important role in implementing any sensor in the commercial field. Considering the same, we carried out the selectivity of different oxidizing and reducing gases like CO, NH$_3$, H$_2$S, and NO$_2$ at 50 °C for 150 ppm H$_2$ gas concentration, and the observed responses are 3.43, 3.51, 6.43, and 4.38%, respectively. These are much lower than the response observed for H$_2$ gas, ∼10.36%. These results are summarized in Figure 8a. It is observed that fabricated pristine
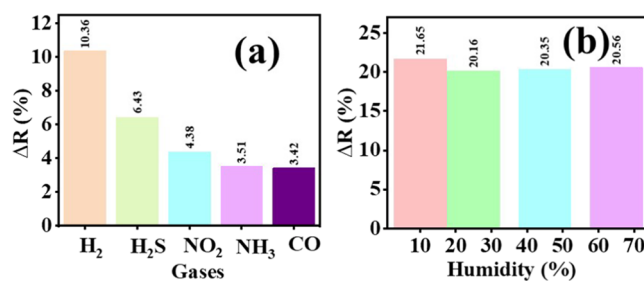
Figure 8. (a) Relative selectivity of ZnO NRs toward hydrogen gas compared to H$_2$S, NO$_2$, NH$_3$, and CO gases at 50 °C with 150 ppm gas concentration and (b) effect of humidity on ZnO NRs at 150 °C with 150 ppm gas concentration.

ZnO NRs are relatively more selective toward H$_2$ gas. The relative sensitivity of H$_2$S gas is also significant and is attributed to its reducing characteristics. However, a considerable change is easily discernible for hydrogen gas. All other reducing and oxidizing gases showed relatively much smaller (approximately half or lower) sensitivities with respect to H$_2$ gas. We also investigated the effect of relative humidity on the response by varying it from 10 to 65% at 150 °C for 150 ppm gas concentration. We intentionally selected the higher temperature to understand the impact of external humidity on hydrogen-sensing response as water vapors were condensing on the bottom surface of the test chamber at lower temperatures without changing the humidity of the test chamber. The results are summarized in Figure 8b and do not exhibit any significant change in response over 10−65% relative humidity. The insensitivity to the relative humidity suggests that the pristine ZnO NR-based sensor is suitable for hydrogen sensing even under moist conditions.

Impedance Measurement. We also carried out impedance measurements for ZnO nanorod-based sensors in the absence and presence of a target gas at both 50 and 100 °C to understand the change in impedance and any interface contribution in the sensing of a target gas. The measurements are carried out at 0.05 V bias voltage from 100 Hz to 1 MHz. The transfer of electron processes is observed in ZnO

Table 2. Sheet Resistance (R_s or R_Ω), Charge Transfer Resistance (R_{ct} or R_p), and Double-Layer Capacitance (C_{dl}) Values, as Derived from Impedance Fitting for ZnO Nanorods with and without H_2 Gas Exposure

	50 °C					100 °C				
element	before gas exposure	25 ppm	100 ppm	150 ppm	after gas exposure	before gas exposure	25 ppm	100 ppm	150 ppm	after gas exposure
R_{ct} (kΩ)	3.45	3.38	3.29	3.37	3.56	3.39	3.03	2.96	2.99	3.25
R_s (Ω)	439	296	326	364	388	326	174	254	280	265
C_{dl} (nf)	82.7	107	96.9	88.6	73.3	67.7	205	120	90	110

Table 3. Sensing Characteristics for Doped, Composite, and Heterostructures Based on ZnO, Including the Present Work, on Pristine ZnO Nanorods[a]

material	gas concentration (ppm)	temperature (°C)	response (%)	ref
rGO-loaded Ni-doped ZnO	100	110	63.8	6[a]
ZnO:Co	3000	150	53.7	18[b]
ZnO P−N junction	500	400	4.5	42[c]
ZnO-SnO$_2$	0.2−10	350	80−100	48[c]
ZnO:Eu	100	300	115	49[d]
ZnO:Pd	100	300	2.7	50[c]
Pd/ZnO	100	RT	1.3×10^4	51[d]
Pd/ZnO nanorods	7	175	38	25[a]
Pd/ZnO	200 cm^3/min	150	0.75	52[e]
rGO:ZnO	500	250	30	53[e]
Pd@ZnO nanoflower	50	RT	70	54[a]
ZnO/rGO	200	400	18	24[d]
Eu:ZnO	100	250	115	55[d]
Pt@ZnO	15	250	4.8	27[d]
ZnO nanorods	1000	250	4000	56[b]
ZnO-coated Sb$_2$O$_3$	3000	100	2.9	57
ZnO nanorods	12.5−150	50, 100, 150	Table 1	present work

[a]The symbols (a) to (f) represent the response calculation approaches used to compute the respective responses and are defined as (a) $= (R_a - R_g)/R_a$; (b) $= \frac{(I_{gas} - I_{air})}{I_{air}} \times 100$; (c) $= R_a - R_g$; (d) $I_g - I_a$; and (e) $= \frac{(G_g - G_a)}{G_a} \times 100$. Here, R_a and R_g are, respectively, resistances; I_{gas} (I_g) and I_{air} (I_a) are, respectively, currents, and G_g and G_a are, respectively, conductances of devices under air and target gas.

nanorods from electrochemical impedance spectroscopy in the 100 Hz to 1 MHz frequency range in the presence of a target gas for different concentrations at 50 and 100 °C at 0.05 V applied bias voltage. This low external voltage is applied to overcome the overpotential during the experiment. The impedance data is analyzed using Nyquist plots for 50 and 100 °C (see Supporting Figure S2). The data are fitted with an equivalent circuit, as shown in the inset, consisting of resistance in series, known as sheet resistance (R_1), together with a parallel combination of resistance, defined as the charge transfer resistance (R_{ct}), as well as capacitance, defined as the double-layer capacitance (C_{dl}) of the active layer. The sheet resistance is attributed to the contact resistance (Al in the present case), and R_{ct} is attributed to the transfer of charge (for both electronic and ionic charges), causing electrode−electrolyte interface resistance. In contrast, C_{dl} is attributed to the onset of double-layer capacitance at the electrode material, i.e., ZnO and electrolyte interface. The high-frequency region in the Nyquist plot provides information about the bulk properties, whereas the mid- and low-frequency regions explain the grain boundary and electrodes, i.e., contacts.[18] The postexposure measurements suggest that residual hydrogen molecules are still adsorbed on ZnO nanorods, as these measurements are carried out after a few minutes of hydrogen exposure. Further, the circuit parameters extracted after fitting the experimental impedance data are evaluated and summarized in Table 2 for different gas concentrations, including pre- and post-gas detection con-

ditions. We observed that the sheet resistance (R_1) reduces on increasing the operating temperature. This reduction in sheet resistance is attributed to a decrease in barrier height due to charge carriers' injection, which enhances the electrical conductivity at a higher temperature. The defect energy, especially for oxygen vacancies, also reduces with increasing temperature.[44]

The charge transfer resistance R_{ct} reduces on introducing higher gas temperatures and recovers back to the initial state approximately after exposure to hydrogen gas, Table 2. Initially, the oxygen molecules trap conduction electrons during the exposure of ZnO NRs to the ambient condition.[45] It induces the surface depletion layer, developing the potential barrier and thus reducing the carriers in the conduction band of ZnO NRs. Interestingly, the exposure of ZnO NRs to H_2 gas results in the removal of surface oxygen atoms, thus releasing the trapped electrons back to CB of ZnO NRs. It reduces the potential barrier and enhances the electrical conduction in ZnO NRs, which reduces Rct. The negatively charged ions may increase at the ZnO NR boundaries due to the adsorption of H_2 at ZnO NR edges, affecting the depletion layer of the material. It will change the corresponding sheet resistance (R_s). Moreover, there is no significant change in C_{dl} values, suggesting that H_2 gas mainly affects the surface of ZnO NRs.[28,46,47] Finally, we also compared the performance of various hydrogen gas-sensing materials with the present pristine ZnO NR response. The optimal response is summarized in Table 3 for different materials with respective
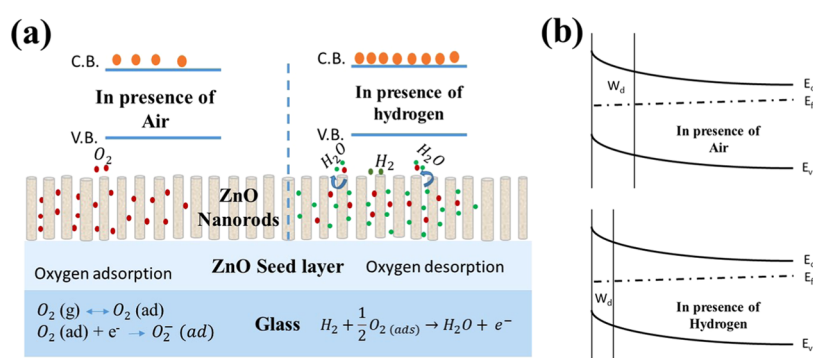
Figure 9. (a) Schematic diagram explaining the H_2-sensing mechanism of sensors based on a metal oxide semiconductor in the presence of air and hydrogen gas together with the respective adsorption processes of oxygen and its reaction with hydrogen, generating conduction band electrons and (b) Enegy band diagrams in presence of air and hydrogen, explaining the reduction in delpetion width W_d.
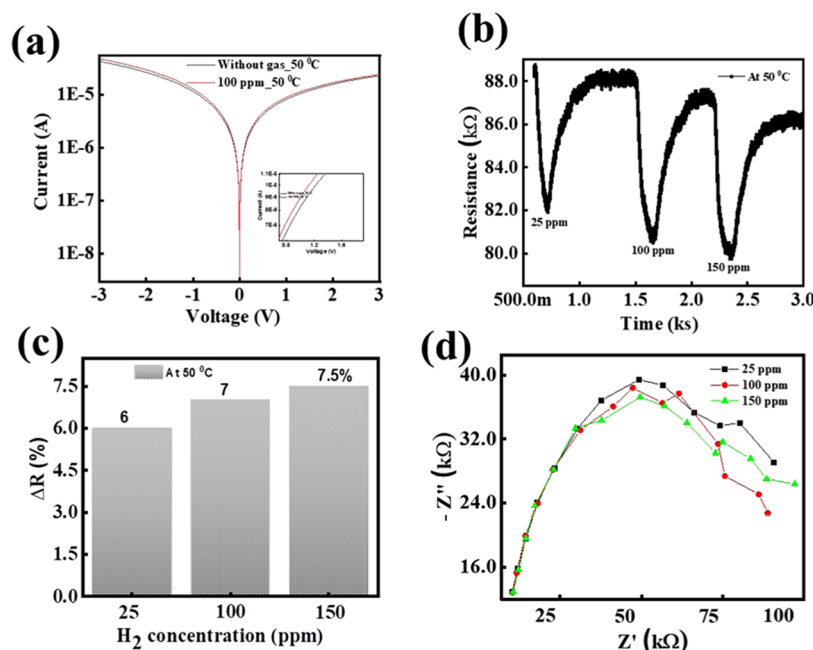
Figure 10. H_2 gas-sensing characteristics on ZnO nanorods after 10 months from initial measurements: (a) $I-V$ measurement; (b) response at 50 °C for 25, 100, and 150 ppm concentrations; (c) histogram representing the response of ZnO nanorods; and (d) impedance for ZnO NRs at 50 °C and 100 at 25, 100, and 150 ppm concentrations.

gas concentrations, operating temperature, and response together with these characteristics for the present work. The response is usually investigated at higher temperatures, ranging from 110 to 400 °C, and some responses are even reported at much higher concentrations like 500 and 3000 ppm hydrogen. The response of the palladium-decorated ZnO system is relatively higher compared to other doped or composite ZnO-based systems, which is also summarized in Table 3 for comparison. The enhanced response is attributed to the catalytic activity of hydrogen adsorption. The present work demonstrates the catalytic free hydrogen adsorption in ZnO NRs at much lower temperatures, i.e., 50–100 °C, with high response even for 25 ppm hydrogen concentration.

Sensing Mechanism. The sensing response in pristine ZnO nanorods can be understood in terms of adsorption and desorption on the surface of ZnO NRs. The room-temperature PL data substantiates the presence of oxygen vacancy or oxygen defect state in ZnO nanorods. Further, these oxygen vacancies or chemisorbed oxygen molecules help in achieving adsorption or desorption at the surface of the device in the

presence of any target gas. It changes physical properties such as current or resistance, which is attributed to the change in conduction band carriers of ZnO NRs. The schematic of oxygen molecule adsorption and desorption under ambient and target gas exposure is explained in Figure 9a. The adsorption of oxygen molecules on the ZnO NR surface extracts an electron from the conduction band, thus depleting the carriers, exhibiting a higher resistance, as explained schematically in Figure 9a using reduced electrons in conduction.[58] The respective oxygen adsorption reactions are also summarized in Figure 9, which can also be understood using a band diagram, as shown in Figure 9b. Moreover, on introducing the target gas hydrogen, the desorption of the oxygen molecule takes place, as explained schematically in Figure 9a, with probable chemical reactions for oxygen adsorption and electron generation in presence of air and hydrogen. This process releases electrons to the conduction band of ZnO NRs, thus reducing the resistivity of ZnO NRs, as explained schematically with relatively larger electrons in the conduction band. On further exposure to the normal ambient

conditions, ZnO NRs regain their initial resistance because of the desorption of water molecules from the ZnO NR surface. The respective change in the conduction band of ZnO NRs is explained schematically in Figure 9a for both adsorption and desorption of oxygen during these processes.[10,59−61] The presence of nanopores in the synthesized ZnO NRs with a large surface-to-volume ratio may provide more active sites for oxygen adsorption and thus be responsible for more hydrogen adsorption, showing enhanced sensing response.[62]

Robustness of ZnO NR-Based Sensors. The stability of any sensing device is very important for its practical uses. Considering the same, we evaluated the sensing response stability of ZnO NR-based hydrogen sensors after 10 months or more from initial device sensing experiments immediately after the fabrication of these devices. The current−voltage (I−V) measurements are performed at 50 °C in the presence of air and hydrogen gas at 25, 100, and 150 ppm concentrations, and the recorded I−V characteristics are shown in Figure 10a for 50 °C. Significant changes in resistance at 2 V biased voltage are noticed (inset, Figure 10a) after introducing the hydrogen target gas on ZnO NRs. The on and off characteristics of ZnO NRs are shown in Figure 10b for 25, 100, and 150 ppm gas concentrations at 50 °C. The change in response to changing gas concentration for 50 °C is summarized in Figure 10c. An increase in response is observed with increasing gas concentration. We also carried out impedance measurements at 50 and 100 °C for different gas concentrations (Figure 10d). A slight increase in charge transfer resistance (R_{ct}) is noticed compared to the former R_{ct} values for ZnO nanorods. These results are nearly identical to those of initial measurements, suggesting the robustness of ZnO NRs for gas-sensing measurements without any reduction in performance.

CONCLUSIONS

We successfully demonstrated the low-cost hydrothermal synthesis of highly textured ZnO NRs. These NRs are vertically aligned to the substrates. The measured length and diameter are 6 μm and 200−250 nm, respectively. Aluminum is deposited as 150 nm electrodes in interdigitated geometries. The devices showed relatively better hydrogen-sensing responses at much lower temperatures, i.e., 50 and 100 °C. At higher temperatures, i.e., 150 °C, the devices showed the maximum response, which may further be improved by increasing the operating temperature. The minimum response observed is 5.28% for 12.5 ppm hydrogen concentration at 50 °C, whereas the maximum of ∼21.65% is noticed for 150 ppm at 150 °C. The sensing response of the device is insensitive to the relative humidity of the environment. The relative selectivity for hydrogen is maximum for the pristine ZnO NRs over other reducing/oxidizing gases. More interestingly, the sensing response is intact even after 10 months or more exposure of these devices to normal ambient conditions. These results suggest that pristine ZnO nanorods with Al metal contacts can be used as robust, low-temperature hydrogen-sensing devices.

ASSOCIATED CONTENT

ⓢ Supporting Information

The Supporting Information is available free of charge at https://pubs.acs.org/doi/10.1021/acsomega.2c02510.

> Optical, vibrational, impedance, and nitrogen adsorption/desorption isotherms for ZnO NRs (PDF)

AUTHOR INFORMATION

Corresponding Author

Ambesh Dixit − *Advances Material and Device (A-MAD) Laboratory, Department of Physics, Indian Institute of Technology, Jodhpur 342037 Rajasthan, India;* ⊙ orcid.org/0000-0003-2285-0754; Email: ambesh@iitj.ac.in

Authors

Chandra Prakash − *Advances Material and Device (A-MAD) Laboratory, Department of Physics, Indian Institute of Technology, Jodhpur 342037 Rajasthan, India*

Rajneesh Chaurasiya − *Advances Material and Device (A-MAD) Laboratory, Department of Physics, Indian Institute of Technology, Jodhpur 342037 Rajasthan, India;* Present Address: R.C.: Department of Materials Science and Engineering, National Cheng Kung University, Tainan 701, Taiwan; ⊙ orcid.org/0000-0002-3301-2089

Abhijeet J. Kale − *Advances Material and Device (A-MAD) Laboratory, Department of Physics, Indian Institute of Technology, Jodhpur 342037 Rajasthan, India*

Complete contact information is available at:
https://pubs.acs.org/10.1021/acsomega.2c02510

Notes

The authors declare no competing financial interest.

REFERENCES

(1) Hu, K.; Wang, F.; Shen, Z.; Liu, H.; Xiong, J. Ternary Heterojunctions Synthesis and Sensing Mechanism of Pd/ZnO−SnO$_2$ Hollow Nanofibers with Enhanced H$_2$ Gas Sensing Properties. *J. Alloys Compd.* **2021**, *850*, No. 156663.

(2) Öztürk, S.; Kilinç, N.; Torun, I.; Kösemen, A.; Şahin, Y.; Öztürk, Z. Z. Hydrogen Sensing Properties of ZnO Nanorods: Effects of Annealing, Temperature and Electrode Structure. *Int. J. Hydrogen Energy* **2014**, *39*, 5194−5201.

(3) Nakate, U. T.; Ahmad, R.; Patil, P.; Bhat, K. S.; Wang, Y.; Mahmoudi, T.; Yu, Y. T.; Suh, E.-k.; Hahn, Y.-B. High Response and Low Concentration Hydrogen Gas Sensing Properties Using Hollow ZnO Particles Transformed from Polystyrene@ZnO Core-Shell Structures. *Int. J. Hydrogen Energy* **2019**, *44*, 15677−15688.

(4) Gu, H.; Wang, Z.; Hu, Y. Hydrogen Gas Sensors Based on Semiconductor Oxide Nanostructures. *Sensors* **2012**, *12*, 5517−5550.

(5) Katoch, A.; Abideen, Z. U.; Kim, H. W.; Kim, S. S. Grain-Size-Tuned Highly H$_2$-Selective Chemiresistive Sensors Based on ZnO-SnO$_2$ Composite Nanofibers. *ACS Appl. Mater. Interfaces* **2016**, *8*, 2486−2494.

(6) Bhati, V. S.; Ranwa, S.; Rajamani, S.; Kumari, K.; Raliya, R.; Biswas, P.; Kumar, M. Improved Sensitivity with Low Limit of Detection of a Hydrogen Gas Sensor Based on rGO-Loaded Ni-Doped ZnO Nanostructures. *ACS Appl. Mater. Interfaces* **2018**, *10*, 11116−11124.

(7) Majhi, S. M.; Rai, P.; Yu, Y. T. Facile Approach to Synthesize Au@ZnO Core-Shell Nanoparticles and Their Application for Highly Sensitive and Selective Gas Sensors. *ACS Appl. Mater. Interfaces* **2015**, *7*, 9462−9468.

(8) Caglar, M.; Ilican, S.; Caglar, Y. Influence of Dopant Concentration on the Optical Properties of ZnO: In Films by Sol-Gel Method. *Thin Solid Films* **2009**, *517*, 5023−5028.

(9) Hyodo, T.; Goto, T.; Takamori, M.; Ueda, T.; Shimizu, Y. Effects of Pt Loading onto SnO$_2$ Electrodes on CO-Sensing Properties and Mechanism of Potentiometric Gas Sensors Utilizing an Anion-Conducting Polymer Electrolyte. *Sens. Actuators, B* **2019**, *300*, No. 127041.

(10) Ji, H.; Zeng, W.; Li, Y. Gas Sensing Mechanisms of Metal Oxide Semiconductors: A Focus Review. *Nanoscale* **2019**, *11*, 22664−22684.

(11) Chen, Y.; Zhang, Y.; Zhang, H.; Chen, C. Design and Evaluation of Cu-Modified ZnO Microspheres as a High Performance Formaldehyde Sensor Based on Density Functional Theory. *Appl. Surf. Sci.* **2020**, *532*, No. 147446.

(12) Liu, Q.; Yasui, T.; Nagashima, K.; Yanagida, T.; Hara, M.; Horiuchi, M.; Zhu, Z.; Takahashi, H.; Shimada, T.; Arima, A.; Baba, Y. Ammonia-Induced Seed Layer Transformations in a Hydrothermal Growth Process of Zinc Oxide Nanowires. *J. Phys. Chem. C* **2020**, *124*, 20563−20568.

(13) Yang, X.; Wang, W.; Xiong, J.; Chen, L.; Ma, Y. ZnO:Cd Nanorods Hydrogen Sensor with Low Operating Temperature. *Int. J. Hydrogen Energy* **2015**, *40*, 12604−12609.

(14) Rahman, F. Zinc Oxide Light-Emitting Diodes: A Review. *Opt. Eng.* **2019**, *58*, No. 1.

(15) Lee, J. H.; Park, B. O. Transparent Conducting ZnO:Al, In and Sn Thin Films Deposited by the Sol-Gel Method. *Thin Solid Films* **2003**, *426*, 94−99.

(16) Mondal, B.; Basumatari, B.; Das, J.; Roychaudhury, C.; Saha, H.; Mukherjee, N. ZnO-SnO$_2$ Based Composite Type Gas Sensor for Selective Hydrogen Sensing. *Sens. Actuators, B* **2014**, *194*, 389−396.

(17) Nunes, P.; Fortunato, E.; Tonello, P.; Braz Fernandes, F.; Vilarinho, P.; Martins, R. Effect of Different Dopant Elements on the Properties of ZnO Thin Films. *Vacuum* **2002**, *64*, 281−285.

(18) Sett, D.; Basak, D. Highly Enhanced H$_2$ Gas Sensing Characteristics of Co:ZnO Nanorods and Its Mechanism. *Sens. Actuators, B* **2017**, *243*, 475−483.

(19) Gupta, D.; Dutta, D.; Kumar, M.; Barman, P. B.; Som, T.; Hazra, S. K. Temperature Dependent Dual Hydrogen Sensor Response of Pd Nanoparticle Decorated Al Doped ZnO Surfaces. *J. Appl. Phys.* **2015**, *118*, No. 164501.

(20) Hembram, K.; Rao, T. N.; Ramakrishana, M.; Srinivasa, R. S.; Kulkarni, A. R. Influence of CaO Doping on Phase, Microstructure, Electrical and Dielectric Properties of ZnO Varistors. *J. Alloys Compd.* **2020**, *817*, No. 152700.

(21) Abun, A.; Huang, B.; Saravanan, A.; Kathiravan, D.; Hong, P. Exfoliated MoSe$_2$ Nanosheets Doped on the Surface of ZnO Nanorods for Hydrogen Sensing Applications. *ACS Appl. Nano Mater.* **2020**, *3*, 12139−12147.

(22) Fan, F.; Zhang, J.; Li, J.; Zhang, N.; Hong, R. R.; Deng, X.; Tang, P.; Li, D. Hydrogen Sensing Properties of Pt-Au Bimetallic Nanoparticles Loaded on ZnO Nanorods. *Sens. Actuators, B* **2017**, *241*, 895−903.

(23) Cittadini, M.; Sturaro, M.; Guglielmi, M.; Resmini, A.; Tredici, I. G.; Anselmi-Tamburini, U.; Koshy, P.; Sorrell, C. C.; Martucci, A. ZnO Nanorods Grown on ZnO Sol-Gel Seed Films: Characteristics and Optical Gas-Sensing Properties. *Sens. Actuators, B* **2015**, *213*, 493−500.

(24) Das, S.; Roy, S. Sensor Materials Performance Improvement of N-ZnO / p-RGO Heterojunction Based Room Temperature Hydrogen Gas Sensor. *IEEE Sens. Lett.* **2021**, *5*, 1−4.

(25) Kumar, M.; Bhati, V. S.; Ranwa, S.; Singh, J.; Kumar, M. Pd/ZnO Nanorods Based Sensor for Highly Selective Detection of Extremely Low Concentration Hydrogen. *Sci. Rep.* **2017**, *7*, No. 236.

(26) Agarwal, S.; Kumar, S.; Agrawal, H.; Moinuddin, M. G.; Kumar, M.; Sharma, S. K.; Awasthi, K. An Efficient Hydrogen Gas Sensor Based on Hierarchical Ag / ZnO Hollow Microstructures. *Sens. Actuators, B* **2021**, *346*, No. 130510.

(27) Cheng, I. K.; Lin, C. Y.; Pan, F. M. Gas sensing behaviour of ZnO toward H$_2$ at temperatures below 300 °C and its dependence on humidity and Pt-decoration. *Appl. Surf. Sci.* **2021**, *541*, No. 148551.

(28) Lupan, O.; Chai, G.; Chow, L. Novel Hydrogen Gas Sensor Based on Single ZnO Nanorod. *Microelectron. Eng.* **2008**, *85*, 2220−2225.

(29) Jian, L. Y.; Lee, H. Y.; Lee, C. T. Surface Morphology-Dependent Sensitivity of Thin-Film-Structured Indium Oxide-Based NO$_2$ Gas Sensors. *J. Electron. Mater.* **2019**, *48*, 2391−2397.

(30) Lee, J. M.; Lee, W. Effects of Surface Roughness on Hydrogen Gas Sensing Properties of Single Pd Nanowires. *J Nanosci. Nanotechnol.* **2011**, *11*, 2151−2154.

(31) Viter, R.; Iatsunskyi, I.Optical Spectroscopy for Characterization of Metal Oxide Nanofibers. In *Handbook of Nanofibers*; Springer, Cham, 2019; pp 1−35, DOI: 10.1007/978-3-319-42789-8_10-1.

(32) Lupan, O.; Postica, V.; Gröttrup, J.; Mishra, A. K.; De Leeuw, N. H.; Carreira, J. F. C.; Rodrigues, J.; Ben Sedrine, N.; Correia, M. R.; Monteiro, T.; Cretu, V.; Tiginyanu, I.; Smazna, D.; Mishra, Y. K.; Adelung, R. Hybridization of Zinc Oxide Tetrapods for Selective Gas Sensing Applications. *ACS Appl. Mater. Interfaces* **2017**, *9*, 4084−4099.

(33) Ghosh, H.; Sadeghimakki, B.; Sivoththaman, S. Enhancement of UV Emission and Optical Bandgap of ZnO Nanowires via Doping and Post-Growth Annealing. *Mater. Res. Express* **2020**, *7*, No. 035013.

(34) Khan, M.; Naqvi, A. H.; Ahmad, M. Comparative Study of the Cytotoxic and Genotoxic Potentials of Zinc Oxide and Titanium Dioxide Nanoparticles. *Toxicol. Rep.* **2015**, *2*, 765−774.

(35) Sowri Babu, K.; Ramachandra Reddy, A.; Sujatha, C.; Venugopal Reddy, K.; Mallika, A. N. Synthesis and Optical Characterization of Porous ZnO. *J. Adv. Ceram.* **2013**, *2*, 260−265.

(36) Achour, A.; Islam, M.; Vizireanu, S.; Ahmad, I.; Akram, M. A.; Saeed, K.; Dinescu, G.; Pireaux, J. J. Orange/Red Photoluminescence Enhancement upon Sf$_6$ Plasma Treatment of Vertically Aligned Zno Nanorods. *Nanomaterials* **2019**, *9*, No. 794.

(37) Das, N. C.; Biswas, S.; Sokol, P. E. The Photovoltaic Performance of ZnO Nanorods in Bulk Heterojunction Solar Cells. *J. Renewable Sustainable Energy* **2011**, *3*, No. 033105.

(38) Ma, Y.; Choi, T. W.; Cheung, S. H.; Cheng, Y.; Xu, X.; Xie, Y. M.; Li, H. W.; Li, M.; Luo, H.; Zhang, W.; So, S. K.; Chen, S.; Tsang, S. W. Charge Transfer-Induced Photoluminescence in ZnO Nanoparticles. *Nanoscale* **2019**, *11*, 8736−8743.

(39) Kołodziejczak-radzimska, A.; Markiewicz, E.; Jesionowski, T. Structural Characterisation of ZnO Particles Obtained by the Emulsion Precipitation Method. *J. Nanomater.* **2012**, *2012*, 1−9.

(40) Polarz, S.; Smarsly, B. Nanoporous Materials. *J. Nanosci. Nanotechnol.* **2002**, *2*, 581−612.

(41) Wu, Z.; Li, Z.; Li, H.; Sun, M.; Han, S.; Cai, C.; Shen, W.; Fu, Y. Ultrafast Response / Recovery and High Selectivity of the H$_2$S Gas Sensor Based on α - Fe$_2$O$_3$ Nano-Ellipsoids from One-Step Hydrothermal Synthesis. *ACS Appl. Mater. Interfaces* **2019**, *11*, 12761−12769.

(42) Zhang, H.; Li, Z.; Liu, L.; Xu, X.; Wang, Z.; Wang, W.; Zheng, W.; Dong, B.; Wang, C. Enhancement of Hydrogen Monitoring Properties Based on Pd-SnO$_2$ Composite Nanofibers. *Sens. Actuators, B* **2010**, *147*, 111−115.

(43) Daryakenari, A. A.; Apostoluk, A.; Delaunay, J. J. Catalytic Behaviour of Ultrafine Pt on the Gas Sensor of ZnO Nanoparticles. 2017, pp 302−303.

(44) Kim, H.; Pak, Y.; Jeong, Y.; Kim, W.; Kim, J.; Jung, G. Y. Amorphous Pd-Assisted H$_2$ Detection of ZnO Nanorod Gas Sensor with Enhanced Sensitivity and Stability. *Sens. Actuators, B* **2018**, *262*, 460−468.

(45) Nguyen, C. P. T.; La, P. P. H.; Trinh, T. T.; Le, T. A. H.; Bong, S.; Jang, K.; Ahn, S.; Yi, J. Fabrication of ZnO Nanorods for Gas Sensing Applications Using Hydrothermal Method. *J. Nanosci. Nanotechnol.* **2014**, *14*, 6261−6265.

(46) Kashif, M.; Hashim, U.; Ali, E.; Ala'eddin, A. S.; Ali, S. M.; Willander, M. Structural and Impedance Spectroscopy Study of Al-

Doped ZnO Nanorods Grown by Sol-Gel Method. *Microelectron. Int.* **2012**, *29*, 131−135.

(47) Balasubramani, V.; Sureshkumar, S.; Rao, T. S.; Sridhar, T. M. Impedance Spectroscopy-Based Reduced Graphene Oxide-Incorporated ZnO Composite Sensor for H_2S Investigations. *ACS Omega* **2019**, *4*, 9976−9982.

(48) Katoch, A.; Abideen, Z. U.; Kim, H. W.; Kim, S. S. Grain-size-tuned highly H_2-selective chemiresistive sensors based on ZnO−SnO_2 composite nanofibers. *ACS Appl. Mater. Interfaces* **2016**, *8*, 2486−2494.

(49) Lupan, C.; Khaledialidusti, R.; Mishra, A. K.; Postica, V.; Terasa, M. I.; Magariu, N.; Pauporté, T.; Viana, B.; Drewes, J.; Vahl, A.; Faupel, F.; Adelung, R. Pd-Functionalized ZnO:Eu Columnar Films for Room-Temperature Hydrogen Gas Sensing: A Combined Experimental and Computational Approach. *ACS Appl. Mater. Interfaces* **2020**, *12*, 24951−24964.

(50) Kim, J. H.; Mirzaei, A.; Kim, H. W.; Kim, S. S. Pd Functionalization on ZnO Nanowires for Enhanced Sensitivity and Selectivity to Hydrogen Gas. *Sens. Actuators, B* **2019**, *297*, No. 126693.

(51) Lupan, O.; Postica, V.; Adelung, R.; Labat, F.; Ciofini, I.; Schürmann, U.; Kienle, L.; Chow, L.; Viana, B.; Pauporté, T. Functionalized Pd/ZnO Nanowires for Nanosensors. *Phys. Status Solidi RRL* **2018**, *12*, 1−9.

(52) Idris, N. F.; Mohd Yahya, N. A.; Yaacob, M. H.; Idris, A. H.; Harun, S. W.; Saidin, N. Optical Fiber Coated Zinc Oxide (ZnO) Nanorods Decorated with Palladium (Pd) for Hydrogen Sensing. *Opt. Mater.* **2019**, *96*, No. 109291.

(53) Galstyan, V.; Comini, E.; Kholmanov, I.; Faglia, G.; Sberveglieri, G. Reduced Graphene Oxide/ZnO Nanocomposite for Application in Chemical Gas Sensors. *RSC Adv.* **2016**, *6*, 34225−34232.

(54) Jeon, J.-Y.; Park, S.; Ha, T. Functionalization of Zinc Oxide Nano Fl Owers with Palladium Nanoparticles via Microwave Absorption for Room Temperature- Operating Hydrogen Gas Sensors in the Ppb Level. *ACS Appl. Mater. Interfaces* **2021**, *13*, 25082−25091.

(55) Lupan, C.; Khaledialidusti, R.; Mishra, A. K.; Postica, V.; Terasa, M.; Magariu, N.; Pauporte, T.; Viana, B.; Drewes, J.; Vahl, A.; Faupel, F.; Adelung, R. Pd-Functionalized ZnO: Eu Columnar Films for Room-Temperature Hydrogen Gas Sensing: A Combined Experimental and Computational Approach. *ACS Appl. Mater. Interfaces* **2020**, *12*, 24951−24964.

(56) Hassan, J. J.; Mahdi, M. A.; Chin, C. W.; Abu-hassan, H.; Hassan, Z. Sensors and Actuators B: Chemical A High-Sensitivity Room-Temperature Hydrogen Gas Sensor Based on Oblique and Vertical ZnO Nanorod Arrays. *Sens. Actuators, B* **2013**, *176*, 360−367.

(57) Pradeep, N.; Tamil, G.; Venkatraman, U.; Le, Q.; Van; Kwan, S.; Pandiaraj, S.; Alodhayb, A. Development and Investigation of the Fl Exible Hydrogen Sensor Based on ZnO-Decorated Sb $_2O_3$ Nanobelts. *Mater. Today Chem.* **2021**, *22*, No. 100576.

(58) Ueda, T.; Boehme, I.; Hyodo, T.; Shimizu, Y.; Weimar, U.; Barsan, N. Enhanced NO_2-Sensing Properties of Au-Loaded Porous In_2O_3 Gas Sensors at Low Operating Temperatures. *Chemosensors* **2020**, *8*, No. 72.

(59) Ren, Q.; Cao, Y.-Q.; Arulraj, D.; Liu, C.; Wu, D.; Li, W.-M.; Li, A.-D. Review—Resistive-Type Hydrogen Sensors Based on Zinc Oxide Nanostructures. *J. Electrochem. Soc.* **2020**, *167*, No. 067528.

(60) Wetchakun, K.; Samerjai, T.; Tamaekong, N.; Liewhiran, C.; Siriwong, C.; Kruefu, V.; Wisitsoraat, A.; Tuantranont, A.; Phanichphant, S. Semiconducting Metal Oxides as Sensors for Environmentally Hazardous Gases. *Sens. Actuators, B* **2011**, *160*, 580−591.

(61) Chang, C. M.; Hon, M. H.; Leu, I. C. Outstanding H_2 Sensing Performance of Pd Nanoparticle-Decorated ZnO Nanorod Arrays and the Temperature-Dependent Sensing Mechanisms. *ACS Appl. Mater. Interfaces* **2013**, *5*, 135−143.

(62) Shen, Y.; Yamazaki, T.; Liu, Z.; Meng, D.; Kikuta, T.; Nakatani, N. In Fl Uence of Effective Surface Area on Gas Sensing Properties of WO_3 Sputtered Thin Fi Lms. *Thin Solid Films* **2009**, *517*, 2069−2072.